

Terahertz Photonics on a Chip: Monolithically Integrated Terahertz Optoelectronics based on Quantum Well Structures

Yifan Zhao^{1,2}, Shahed-E- Zumrat^{1,2}, Mona Jarrahi^{1,2*}

¹Electrical and Computer Engineering Department, University of California; Los Angeles, 90095, USA.

²California NanoSystems Institute, University of California; Los Angeles, 90095, USA.

*Corresponding author. Email: mjarrahi@ucla.edu

Abstract: We introduce a monolithically integrated terahertz optoelectronics (MITO) platform that uses quantum well (QW) structures to enable tunable terahertz signal generation and detection on a single chip. Through photomixing in QW PIN photodiodes, the MITO platform achieves terahertz generation and detection with substantially enhanced power efficiency and sensitivity over previous devices. By integrating semiconductor optical amplifiers, lasers, modulators, filters, demultiplexers, and other passive optical components with photomixers using commercially available photonic integrated circuit foundry processes, this platform supports the development of compact, scalable terahertz systems capable of high-speed data transfer, spectroscopy, and hyperspectral imaging. This advancement positions terahertz technology for widespread use, facilitating practical applications across remote sensing, communications, and medical diagnostics within portable devices.

The terahertz frequency range unlocks unique functionalities for remote sensing, communication, and imaging. Radar systems operating at these frequencies significantly enhance surveillance resolution and allow for smaller apertures, ideal for mobile applications like self-driving vehicles, drone avionics, security screening, and human-computer interfaces. Additionally, terahertz carriers enable high-data-rate communication at frequency bands not yet allocated to specific services, opening opportunities for novel communication solutions. Moreover, many rotational and vibrational frequencies of chemicals fall within the terahertz range, facilitating remote chemical identification through spectroscopy and spectrometry. Another advantage of terahertz frequencies is their ability to penetrate optically opaque materials more effectively than visible light. This property allows for observations in visually inaccessible environments, offering significant potential for non-destructive quality control across food, energy, automotive, and pharmaceutical sectors. Furthermore, several water absorption lines lie in the terahertz range, where biological tissue scattering is minimal compared to optical waves. This quality enhances image contrast for differentiating between benign and malignant tissues, identifying inflammation, and mapping blood vessels—all without posing a health risk. Together, these distinctive characteristics make the terahertz frequency range exceptionally promising for applications across industries and scientific fields.

Although the unique potential of the terahertz frequency range is well recognized, the relatively low performance, high cost, and bulky design of conventional terahertz systems continue to hinder their adoption across many applications. Unlike integrated circuits, whose operation frequency is constrained by transistor cutoff frequencies, parasitic elements, and interconnect losses, optical systems provide distinct advantages for handling high-frequency signals, including simpler signal distribution, multiplexing, lower propagation losses, and broad modulation and amplification bandwidths ($I-I_0$). As a result, optoelectronic approaches, particularly those based on photoconductive antennas and nonlinear optical processes, have been developed to implement essential components for terahertz imaging, sensing, and communication systems—capabilities that are beyond the reach of conventional integrated circuits.

Despite their potential, these optoelectronic techniques remain limited in mainstream applications due to their complexity, high costs, and bulky nature. These limitations stem from the reliance on specialized optical sources, amplifiers, modulators, photoconductors, photodiodes, and nonlinear crystals that are incompatible with standard integrated photonics. Additionally, these devices require independent packaging and control electronics, along with several optical components to couple the optical pump beam to the device's active area. Without monolithically integrated ultrafast optoelectronic systems, implementing complex imaging, spectroscopy, spectrometry, and communication modalities that rely on arrays of sources and detectors with independent amplitude, phase, and frequency control—such as phased arrays and focal plane arrays—is impractical. For truly transformative advancements in terahertz technology, a monolithically integrated terahertz optoelectronics (MITO) platform is essential. Such a platform would address the practical challenges of large size, high cost, and system complexity, enabling terahertz technology to move beyond the lab into widespread, real-world applications.

Previous work on waveguide-coupled terahertz sources and detectors has required external lasers to function (11–19). On the other hand, the demonstrated integrated terahertz optoelectronics has relied on complex fabrication processes, such as multiple epitaxial growth steps to achieve monolithic integration of uni-traveling-carrier photodiodes with optical pump lasers, semiconductor optical amplifiers (SOAs), and modulators (20), as well as bonding multiple III-V stacks onto a silicon photonics chip for the heterogeneous integration of lasers, modulators, and photodiodes (21). Beyond scalability issues, these integrated terahertz optoelectronics schemes have been limited to generating signals up to ~100 GHz, without demonstrating high-frequency signal detection. Here, we introduce a MITO platform that leverages the quantum-confined Stark effect, stimulated photon emission, interband photon absorption, and ultrafast carrier dynamics in quantum well (QW) structures to create a fully integrated terahertz optoelectronic system on a single substrate, eliminating the need for regrowth or bonding processes. In a prototype fabricated on a GaAs/AlGaAs QW substrate, we demonstrate frequency-tunable terahertz generation and detection across the 100–500 GHz range, achieving both higher terahertz generation efficiency and improved terahertz detection sensitivity compared to the state-of-the-art (see Supplementary Tables S1 and S2).

Figure 1 illustrates the primary building block of the MITO platform, consisting of multiple QWs embedded within the intrinsic region of a PIN photodiode waveguide. This photodiode can serve various functions—as an optical pump source (Fig. 1A), amplifier (Fig. 1B), intensity modulator (Fig. 1C), phase modulator (Fig. 1D), terahertz source (Fig. 1E), and terahertz detector (Fig. 1F)—based on its operational mode. When current is injected into the photodiode, stimulated photon emission enables it to operate as a laser diode with one or multiple emission wavelengths when using narrowband (e.g. distributed Bragg reflector) or broadband reflecting facets (Fig. 1A) (22, 23). In the absence of highly reflective facets, it can also function as a semiconductor optical amplifier (SOA), amplifying an incoming optical beam as it propagates through the photodiode waveguide (Fig. 1B). Under reverse bias, the quantum-confined Stark effect (24) allows the photodiode to function as an intensity modulator (Fig. 1C) or phase modulator (Fig. 1D), as variations in the QW absorption spectrum enable precise control of light intensity and phase (25, 26).

While QW PIN photodiodes are well established in the realization of lasers, SOAs, and modulators, their application in terahertz signal generation and detection remains largely unexplored. Previous studies have been limited to terahertz generation and detection schemes utilizing intersubband photon absorption in QW PIN photodiodes (27, 28), which cannot be realized through a MITO platform containing all system components. Our recent studies on ultrafast dynamics of carriers generated through interband absorption within QW structures (29) suggest significant potential for developing monolithically integrated terahertz sources and detectors alongside other optoelectronic components. Under reverse bias, which controls interband photon absorption within the QWs, an optical pump beam containing two frequency components separated by a terahertz frequency difference can generate a terahertz photocurrent through photomixing (Fig. 1E). The frequency of the resulting terahertz signal can be tuned by adjusting the optical beat frequency, f_{beat} , with the generated terahertz power scaling quadratically with the induced photocurrent, up to saturation at high reverse bias voltage and optical pump power levels. Similarly, by coupling a received terahertz signal at f_{THz} to the reverse-biased QW PIN photodiode pumped with a terahertz beat frequency,

an intermediate frequency (IF) photocurrent is induced at $|f_{THz} - f_{beat}|$ through photomixing (Fig. 1F). Tuning the optical beat frequency close to the terahertz frequency of interest generates an IF signal that falls within the radio frequency (RF) range, making it compatible with standard RF electronics for straightforward processing.

The frequency response of the photomixing process used for terahertz signal generation and detection is shown in Fig. 1G. This response is primarily influenced by three time constants: τ_{RC} determined by the photodiode's resistance and capacitance; τ_{trans} the carrier transit time from the QWs to the P/N layers; and τ_{QW} the carrier escape time from the QWs (29). The values of τ_{QW} and τ_{trans} are determined by the reverse bias voltage and by the composition and thickness of the heterostructure layers that form the QW PIN photodiode, while τ_{RC} is determined by the photodiode's geometry, which dictates its capacitance and resistance. Thus, careful design of the QW PIN photodiode enables maintaining small τ_{RC} , τ_{QW} , τ_{trans} time constants, reducing frequency roll-off and extending the device's operation within the terahertz range.

Figure 2A illustrates a fabricated terahertz source/detector prototype that generates and detects terahertz signals via photomixing within a GaAs/AlGaAs QW PIN photodiode (see Methods and Supplementary Figs. S1 and S2). The optical pump beam is delivered through a monolithically integrated SOA ridge waveguide on the same substrate. To minimize τ_{RC} while sustaining high quantum efficiency, a tapered photomixer geometry is employed, which reduces parasitic capacitance. Additionally, the P-cladding is partially etched to keep parasitic resistance low. A tapered transition region between the SOA and photomixer mitigates mode mismatch, ensuring efficient light coupling. The photomixer contacts are connected to ground-signal-ground (GSG) pads to detect/apply terahertz signal through standard GSG probes when operating as a terahertz source/detector. The first prototype features a 12- μm -long photomixer with a tapered waveguide width varying from 3 μm to 0.5 μm terminated with an output probe impedance of 50 Ω . This configuration is estimated to offer a τ_{RC} of 1.55 ps and 56% optical absorption in the photomixer active region at a 3 V reverse bias (see Supplementary Figs. S3 and S4). Figure 2B shows the optical mode transition from the SOA to the photomixer, demonstrating how the tapered design focuses light into the photomixer while preserving high quantum efficiency. To electrically isolate the SOA from the photomixer, the tapered transition region is partially proton-implanted, providing a resistance of 1 G Ω for a 5 μm -long implanted region. Figure 2C illustrates the transmitted optical power through varying lengths of the implanted region, indicating an optical loss of 0.21 dB/ μm .

The device characterization is carried out in two stages. In the first stage, two commercially available lasers, operating at approximately 809 nm, are used to characterize both the SOA and the monolithically integrated terahertz source/detector. In the second stage, a Fabry-Perot laser, fabricated on the same substrate, is employed to demonstrate the monolithically integrated terahertz optoelectronic platform. Figure 2D shows the output power of a 1-mm-long SOA as a function of the SOA pump current, with an input optical power of 0.15 mW, indicating a threshold current of approximately 60 mA, and a free-space-coupled maximum output power of 8 mW at a pump current of 130 mA (see Methods). The relative intensity of the SOA input and output spectra for an optical beat frequency of 300 GHz is shown in the insets of Fig. 2D. The slight imbalance between the two amplified tones is attributed to the wavelength dependence of the SOA gain, as evidenced by the amplified spontaneous emission (ASE) spectrum.

Figure 2E shows the generated power from the monolithically integrated terahertz source/detector with the SOA as a function of the photomixer photocurrent at 230 GHz, with an input optical power of 5 mW (see Methods). The photomixer photocurrent can be tuned by both the SOA pump current (i.e., the optical power pumping the photomixer) and the photomixer bias voltage, as shown in the inset of Fig. 2E. While the photomixer photocurrent remains relatively constant for bias voltages between -1.5 V and -3 V (suggesting that the external quantum efficiency reaches its maximum at -1.5 V), the measured terahertz power at the same photocurrent level increases significantly when the bias voltage is increased from -1.5 V to -3 V. This increase is attributed to the reduction in the photo-generated electron/hole energy barrier, which substantially shortens their escape time from the QWs (29). In the absence of frequency roll-off, the generated signal power is expected to follow the theoretical expression of $\frac{1}{2} I_{ph}^2 \times 50\Omega$ (marked by the dashed black line), where I_{ph} is the photomixer photocurrent and 50 Ω is the impedance of the GSG probe. While the measured signal powers adhere to this theoretical slope up to the saturation point at higher photocurrent

levels, the observed deviations from the theoretically predicted powers are due to frequency roll-off, which is caused by device parasitics, carrier transit time, and carrier escape time from the QWs. Figure 2F shows the maximum generated power from the monolithically integrated terahertz source/detector with the SOA as a function of frequency at a bias voltage of -3 V. The 3 MHz 3-dB linewidth of the generated terahertz signal (inset in Fig. 2F) is directly determined by the linewidth of the two free-running lasers used to generate the optical beat signal for these measurements.

Figure 2G shows the conversion gain of the monolithically integrated terahertz source/detector with the SOA when down-converting a 240 GHz signal to 0.8 GHz, with an input optical power of 5 mW (see Methods). Similar to the terahertz generation measurements, the photomixer photocurrent is varied by adjusting the bias voltage and the SOA pump current. The optimal operating conditions for high-sensitivity terahertz detection are determined by considering the tradeoff between the conversion gain and noise performance of the photomixer. The noise is dominated by Johnson-Nyquist noise, shot noise from the photomixer, and amplified spontaneous emission (ASE) from the SOA. As shown in the inset of Fig. 2G, the output noise power of the photomixer exhibits a linear dependence on the photocurrent. The highest signal-to-noise ratio for terahertz detection is achieved at a photomixer bias voltage of -0.7 V and a photocurrent of 0.38 mA. These conditions are therefore used for the subsequent terahertz detection measurements. Figure 2H displays the measured conversion loss and terahertz detection sensitivity (specified as the input-referred noise power density) as a function of frequency under these operating settings. Similar to the terahertz generation mode, the linewidth of the down-converted terahertz signal is directly determined by the linewidth of the two free-running lasers used to generate the optical beat signal in these measurements (Fig. 2H inset).

Leveraging the ultrafast carrier dynamics, the quantum-confined Stark effect, and stimulated photon emission provided by the QW structures, the demonstrated QW photomixer prototype achieves frequency-tunable terahertz generation and detection across the 100-500 GHz range. It even outperforms photomixer-based terahertz sources with free-space optical coupling from an external laser in terms of terahertz generation efficiency (Fig. 3A), while also surpassing prior detectors in terahertz detection sensitivity (Fig. 3B). Notably, the QW photomixer can be monolithically integrated with other optoelectronic system components on the same substrate, without the need for epitaxial regrowth or chip bonding processes. This offers a scalable optoelectronics platform for realizing complex terahertz imaging, spectroscopy, and communication systems on a chip for the first time. Figure 4A illustrates how the introduced MITO platform can be used to realize a terahertz phased-array transceiver for adaptive hyperspectral remote sensing and communication on a chip. As a simple demonstration of the introduced MITO platform, we developed a multi-mode terahertz transmitter using a Fabry-Perot laser, SOA, and photomixer on the same QW substrate (Fig. 4B). The Fabry-Perot laser waveguide is cleaved, and its multi-mode optical emission is edge-coupled to the SOA-integrated photomixer, where the optical tones are amplified and mixed. The resulting multi-mode signal, generated through the photomixing process, contains the beat frequencies of all the optical tone pairs (see Supplementary Fig. S5). This is just a simple example of the many components and systems that can be realized with the MITO platform. Various single-mode and multi-mode lasers, which can be fabricated using photonic integrated circuit (PIC) foundry processes (e.g., InP-based PICs) (30–33), can be integrated on the same QW photodiode substrate along with optical amplifiers, modulators, filters, demultiplexers, and other passive optical components to pump the photomixers, while controlling the phase, intensity, polarization, spectrum, and beam shape of the emitted/detected terahertz radiation.

The monolithically integrated terahertz sources and detectors demonstrated in this work are fabricated on a standard GaAs/AlGaAs QW gain substrate, commonly used in commercially available lasers and SOAs. While the QW structures in this substrate provide a carrier escape time of $\tau_{QW} \approx 0.1$ ps, as shown in Fig. 1G, the carrier transit time, τ_{trans} , and RC time constant, τ_{RC} , can be further reduced by optimizing the photodiode layer thicknesses and photomixer geometry. This allows for significant reduction in frequency roll-off and extends the terahertz generation and detection bandwidth. Moreover, the monolithic integration of the photomixers with lasers, SOAs, and other optical components enables the development of high-performance terahertz sources and detectors based on distributed arrays and traveling-wave architectures—capabilities not previously possible without the MITO platform. Just as integrated

circuit technology revolutionized early, bulky, power-hungry computers into the high-performance microprocessor chips in use today in homes, cars, phones, and health monitoring systems, the introduced MITO platform could bring about a similar technological transformation in the terahertz field. It has the potential to transform terahertz radar, communication, imaging, and sensing systems from expensive, bulky, laboratory-grade setups to scalable, compact, and low-cost microchips for everyday use.

Methods

Fabrication Process: The fabrication process, depicted in Supplementary Fig. S2, begins with lithographic patterning of the SOA top contacts, followed by deposition of a 10/300 nm Cr/Au layer and a liftoff step. The SOA ridge waveguides are then patterned and formed by etching down to the etch-stop layer, utilizing a combination of reactive ion etching and wet etching (see Supplementary Fig. S2a). Following this, the photomixer top contacts are patterned via e-beam lithography, with 10/400 nm Cr/Au deposited and subsequently lifted off. The ion-implantation regions are then defined using photolithography, after which the sample undergoes proton implantation at room temperature, using a dosage of 5×10^{14} cm⁻² at 70 keV and a 7° tilt angle (see Supplementary Fig. S2b). Next, tapered transition regions are defined lithographically and formed by reactive ion etching of a 200-nm-thick AlGaAs layer (see Supplementary Fig. S2c). The SOA and shallow taper regions are then protected with photoresist, and the photomixer top contacts serve as a hard mask for forming the photomixer waveguides via dry etching (see Supplementary Fig. S2d). Subsequently, AlGaAs regions outside the device core are removed through a combination of dry and wet etching to reach the underlying n⁺ GaAs layer. The SOA and photomixer bottom contacts are patterned using photolithography, followed by deposition of a 75/300 nm AuGe/Au layer, liftoff, and rapid thermal annealing at 380 °C for 30 s. An additional 2 μm of Au is then deposited on the photomixer bottom contacts to raise them to the same height as the top contacts, allowing for GSG probe placement (see Supplementary Fig. S2e). Benzocyclobutene (BCB) is subsequently spin-coated, cured, and etched back to planarize the device surface, followed by additional metal deposition in the SOA regions to form the top contact pads (see Supplementary Fig. S2f). BCB is then fully removed from the GSG probe pad areas, along with etching of the underlying n⁺ GaAs layer (see Supplementary Fig. S2f). Another round of BCB spin coating and etch-back follows, exposing both the SOA and photomixer contacts (see Supplementary Fig. S2g). Finally, a 50/450 nm Ti/Au layer is deposited to form the GSG probe pads (see Supplementary Fig. S2h), and the sample is cleaved in preparation for testing.

SOA Characterization Setup: The fabricated SOA samples are cleaved to form 1-mm-long straight ridge waveguides. These SOA waveguides are oriented at a 7° angle relative to the [100] direction of the wafer. To reduce reflections at a wavelength of approximately 809 nm, a 104-nm-thick Al₂O₃ anti-reflection coating is evaporated on both facets of the SOA samples. For initial testing, an optical signal from a DBR laser operating at ~809 nm (Thorlabs DBR808PN) is coupled into the SOA via a lensed fiber. The output beam is then collected using a 4f imaging system and measured with an optical power meter, as shown in Supplementary Fig. S6a. The input optical power coupled into the SOA is estimated based on the measured photocurrent of the SOA under reverse bias. To characterize the spectral properties of the SOA, two optical beams from DBR lasers (both operating at ~809 nm; Thorlabs DBR808PN) are combined through a 50:50 fiber coupler and coupled into the SOA using a lensed fiber. The SOA output beam is directed to an optical spectrum analyzer (OSA) via a lens and fiber collimator, as illustrated in Supplementary Fig. S6b.

Terahertz Source Characterization Setup: The block diagram of the terahertz source characterization setup is shown in Supplementary Fig. S7a. The optical beams from two wavelength-tunable DBR lasers operating at ~809 nm (Thorlabs DBR808PN) with a terahertz beat frequency are combined using a 50:50 fiber coupler and coupled into the SOA through a lensed fiber. Ground-signal-ground (GSG) terahertz probes, covering frequency bands of 140–220 GHz, 220–330 GHz, and 330–500 GHz (FormFactor T-Wave probes), are employed to route the generated terahertz signal to a harmonic mixer (VDI SAX) for down-conversion to an intermediate frequency (IF) around 1.2 GHz. The low-frequency port of the bias-T integrated with the

GSG probes is used to apply the photomixer bias voltage while simultaneously recording its DC photocurrent. The IF signal is then amplified by an RF amplifier (Mini-Circuits ZRL-1150LN+) and split into two paths with an RF splitter (Mini-Circuits ZN2PD1-222-S+), allowing for simultaneous monitoring of the IF spectrum using an electrical spectrum analyzer and measurement of IF power with a calibrated RF power meter (HP 438A power meter with HP 8481A power sensor). To reduce out-of-band noise, a bandpass filter (Pasternack PE8731) is placed before the power detector. The conversion loss of the VDI SAX module is calibrated separately for each frequency band. For operation in the 330–500 GHz band, a WR2.2 active multiplier chain (AMC) (VDI WR9.0SGX-M + WR4.3×2 + WR2.2×2) serves as the source, and its power is measured across the spectral range using a calibrated power meter (VDI PM5B) through a WR2.2 to WR10 taper and a 1-inch WR10 waveguide. The measured power values are corrected to account for taper and waveguide losses based on vendor calibration data. The WR2.2 AMC is then connected to the WR2.2 SAX module, followed by the IF electronics, and IF power is measured with the calibrated RF power meter. The total conversion loss of the setup is determined by comparing the measured IF and terahertz power levels, incorporating the GSG probe losses from vendor calibration data. For operation in the 140–220 GHz band, an Eravant SFA-114174402-06VF-E1 AMC is used as the source, and power is measured over the spectral range using a calibrated power meter (VDI PM5B) through a WR5.1 to WR10 taper and a 1-inch WR10 waveguide. In the 220–330 GHz band, a Millitech AMC-10-RFHB0 AMC connected to a VDI WR10×3 frequency tripler is used as the source, with power measured over the entire spectral range using the same calibrated power meter (VDI PM5B) through a WR3.4 to WR10 taper and a 1-inch WR10 waveguide. The remaining calibration process for these bands follows the procedure described for the 330–500 GHz band.

Terahertz Detector Characterization Setup: The block diagram of the terahertz detector characterization setup is shown in Supplementary Fig. S7b. The optical beams from two wavelength-tunable DBR lasers operating at ~809 nm (Thorlabs DBR808PN), with a terahertz beat frequency, are combined via a 50:50 fiber coupler and coupled into the SOA through a lensed fiber. Ground-signal-ground (GSG) terahertz probes, covering the 140–220 GHz, 220–330 GHz, and 330–500 GHz frequency bands (FormFactor T-Wave probes), are used to apply the terahertz signal generated by the sources described in the previous section for each frequency band. The terahertz power at each frequency is measured using a calibrated power meter (VDI PM5B). The down-converted IF signal, centered around 0.8 GHz, is extracted through the low-frequency port of the bias-T integrated with the GSG probe. The DC and RF components of the IF signal are separated using an RF bias-T (Picosecond Pulse Labs 5541A-104). The RF component is amplified by an RF amplifier (Mini-Circuits ZRL-1150LN+), filtered with a bandpass filter (VBFZ-780-S+), and measured by a calibrated RF power meter (HP 438A power meter with HP 8481A power sensor). Simultaneously, the IF spectrum is monitored with an electrical spectrum analyzer using an RF splitter (Mini-Circuits ZN2PD1-222-S+). The conversion loss of the device is calculated by comparing the terahertz power with the IF power, factoring in the gain of the RF electronics. The calibration process follows the same method as that used for terahertz source characterization.

References

1. T. Nagatsuma, G. Ducournau, C. C. Renaud, Advances in terahertz communications accelerated by photonics. *Nat. Photonics* **10**, 371–379 (2016).
2. S. Koenig, D. Lopez-Diaz, J. Antes, F. Boes, R. Henneberger, A. Leuther, A. Tessmann, R. Schmogrow, D. Hillerkuss, R. Palmer, T. Zwick, C. Koos, W. Freude, O. Ambacher, J. Leuthold, I. Kallfass, Wireless sub-THz communication system with high data rate. *Nat. Photonics* **7**, 977–981 (2013).
3. X. Li, D. Mengu, N. T. Yardimci, D. Turan, A. Charkhesht, A. Ozcan, M. Jarrahi, Plasmonic photoconductive terahertz focal-plane array with pixel super-resolution. *Nat. Photonics* **18**, 139–148 (2024).

4. N. Wang, S. Cakmakyapan, Y.-J. Lin, H. Javadi, M. Jarrahi, Room-temperature heterodyne terahertz detection with quantum-level sensitivity. *Nat. Astron.* **3**, 977–982 (2019).
5. L. Liebermeister, S. Nellen, R. B. Kohlhaas, S. Lauck, M. Deumer, S. Breuer, M. Schell, B. Globisch, Optoelectronic frequency-modulated continuous-wave terahertz spectroscopy with 4 THz bandwidth. *Nat. Commun.* **12**, 1071 (2021).
6. J. Liu, J. Dai, S. L. Chin, X.-C. Zhang, Broadband terahertz wave remote sensing using coherent manipulation of fluorescence from asymmetrically ionized gases. *Nat. Photonics* **4**, 627–631 (2010).
7. N. Couture, W. Cui, M. Lippl, R. Ostic, D. J. J. Fandio, E. K. Yalavarthi, A. Vishnuradhan, A. Gamouras, N. Y. Joly, J.-M. Ménard, Single-pulse terahertz spectroscopy monitoring sub-millisecond time dynamics at a rate of 50 kHz. *Nat. Commun.* **14**, 2595 (2023).
8. J. Dong, P. You, A. Tomasino, A. Yurtsever, R. Morandotti, Single-shot ultrafast terahertz photography. *Nat. Commun.* **14**, 1704 (2023).
9. T. L. Cocker, V. Jelic, M. Gupta, S. J. Molesky, J. A. J. Burgess, G. D. L. Reyes, L. V. Titova, Y. Y. Tsui, M. R. Freeman, F. A. Hegmann, An ultrafast terahertz scanning tunnelling microscope. *Nat. Photonics* **7**, 620–625 (2013).
10. M. Eisele, T. L. Cocker, M. A. Huber, M. Plankl, L. Viti, D. Ercolani, L. Sorba, M. S. Vitiello, R. Huber, Ultrafast multi-terahertz nano-spectroscopy with sub-cycle temporal resolution. *Nat. Photonics* **8**, 841–845 (2014).
11. T. Harter, S. Muehlbrandt, S. Ummethala, A. Schmid, S. Nellen, L. Hahn, W. Freude, C. Koos, Silicon–plasmonic integrated circuits for terahertz signal generation and coherent detection. *Nat. Photonics* **12**, 625–633 (2018).
12. P. Chen, M. Hosseini, A. Babakhani, An integrated germanium-based THz impulse radiator with an optical waveguide coupled photoconductive switch in silicon. *Micromachines* **10**, 367 (2019).
13. J. P. Seddon, M. Natrella, X. Lin, C. Graham, C. C. Renaud, A. J. Seeds, Photodiodes for terahertz applications. *IEEE J. Sel. Top. Quantum Electron.* **28**, 1–12 (2022).
14. A. Herter, A. Shams-Ansari, F. F. Settembrini, H. K. Warner, J. Faist, M. Lončar, I.-C. Benea-Chelmus, Terahertz waveform synthesis in integrated thin-film lithium niobate platform. *Nat. Commun.* **14**, 11 (2023).
15. S. Nellen, S. Lauck, E. Peytavit, P. Szriftgiser, M. Schell, G. Ducournau, B. Globisch, Coherent wireless link at 300 GHz with 160 Gbit/s enabled by a photonic transmitter. *J. Light. Technol.* **40**, 4178–4185 (2022).
16. I.-C. Benea-Chelmus, Y. Salamin, F. F. Settembrini, Y. Fedoryshyn, W. Heni, D. L. Elder, L. R. Dalton, J. Leuthold, J. Faist, Electro-optic interface for ultrasensitive intracavity electric field measurements at microwave and terahertz frequencies. *Optica* **7**, 498–505 (2020).
17. Y. Salamin, I.-C. Benea-Chelmus, Y. Fedoryshyn, W. Heni, D. L. Elder, L. R. Dalton, J. Faist, J. Leuthold, Compact and ultra-efficient broadband plasmonic terahertz field detector. *Nat. Commun.* **10**, 5550 (2019).
18. P. Ma, Y. Salamin, B. Baeuerle, A. Josten, W. Heni, A. Emboras, J. Leuthold, Plasmonically enhanced graphene photodetector featuring 100 Gbit/s data reception, high responsivity, and compact size. *ACS Photonics* **6**, 154–161 (2019).
19. S. Lischke, A. Peczek, J. S. Morgan, K. Sun, D. Steckler, Y. Yamamoto, F. Korndörfer, C. Mai, S. Marschmeyer, M. Fraschke, A. Krüger, A. Beling, L. Zimmermann, Ultra-fast germanium photodiode with 3-dB bandwidth of 265 GHz. *Nat. Photonics* **15**, 925–931 (2021).
20. G. Carpintero, K. Balakier, Z. Yang, R. C. Guzmán, A. Corradi, A. Jimenez, G. Kervella, M. J. Fice, M. Lamponi, M. Chitoui, F. van Dijk, C. C. Renaud, A. Wonfor, E. A. J. M. Bente, R. V. Penty, I. H.

- White, A. J. Seeds, Microwave photonic integrated circuits for millimeter-wave wireless communications. *J. Light. Technol.* **32**, 3495–3501 (2014).
21. J. Hulme, M. Kennedy, R.-L. Chao, L. Liang, T. Komljenovic, J.-W. Shi, B. Szafraniec, D. Baney, J. E. Bowers, Fully integrated microwave frequency synthesizer on heterogeneous silicon-III/V. *Opt. Express* **25**, 2422–2431 (2017).
 22. P. S. Liao, P. Kelley, *Quantum Well Lasers* (Academic Press, 1993).
 23. Y. Arakawa, A. Yariv, Quantum well lasers—Gain, spectra, dynamics. *IEEE J. Quantum Electron.* **22**, 1887–1899 (1986).
 24. D. A. B. Miller, D. S. Chemla, T. C. Damen, A. C. Gossard, W. Wiegmann, T. H. Wood, C. A. Burrus, Band-edge electroabsorption in quantum well structures: the quantum-confined stark effect. *Phys. Rev. Lett.* **53**, 2173–2176 (1984).
 25. T. H. Wood, C. A. Burrus, D. A. B. Miller, D. S. Chemla, T. C. Damen, A. C. Gossard, W. Wiegmann, High-speed optical modulation with GaAs/GaAlAs quantum wells in a *p-i-n* diode structure. *Appl. Phys. Lett.* **44**, 16–18 (1984).
 26. M. Jarrahi, T. H. Lee, D. A. B. Miller, Wideband, Low driving voltage traveling-wave Mach–Zehnder modulator for RF photonics. *IEEE Photonics Technol. Lett.* **20**, 517–519 (2008).
 27. V. Ryzhii, I. Khmyrova, M. Shur, Terahertz photomixing in quantum well structures using resonant excitation of plasma oscillations. *J. Appl. Phys.* **91**, 1875–1881 (2002).
 28. H. Li, W.-J. Wan, Z.-Y. Tan, Z.-L. Fu, H.-X. Wang, T. Zhou, Z.-P. Li, C. Wang, X.-G. Guo, J.-C. Cao, 6.2-GHz modulated terahertz light detection using fast terahertz quantum well photodetectors. *Sci. Rep.* **7**, 3452 (2017).
 29. Y. Zhao, M. Jarrahi, Ultrafast carrier dynamics in multiple quantum well p-i-n photodiodes. arXiv:2411.09183 [physics.optics] (2024).
 30. M. Smit, X. Leijtens, H. Ambrosius, E. Bente, J. Van Der Tol, B. Smalbrugge, T. De Vries, E.-J. Geluk, J. Bolk, R. Van Veldhoven, L. Augustin, P. Thijs, D. D’Agostino, H. Rabbani, K. Lawniczuk, S. Stopinski, S. Tahvili, A. Corradi, E. Kleijn, D. Dzubrou, M. Felicetti, E. Bitincka, V. Moskalenko, J. Zhao, R. Santos, G. Gilardi, W. Yao, K. Williams, P. Stabile, P. Kuindersma, J. Pello, S. Bhat, Y. Jiao, D. Heiss, G. Roelkens, M. Wale, P. Firth, F. Soares, N. Grote, M. Schell, H. Debregeas, M. Achouche, J.-L. Gentner, A. Bakker, T. Korthorst, D. Gallagher, A. Dabbs, A. Melloni, F. Morichetti, D. Melati, A. Wonfor, R. Penty, R. Broeke, B. Musk, D. Robbins, An introduction to InP-based generic integration technology. *Semicond. Sci. Technol.* **29**, 083001 (2014).
 31. H. Hu, F. Da Ros, M. Pu, F. Ye, K. Ingerslev, E. Porto da Silva, M. Nooruzzaman, Y. Amma, Y. Sasaki, T. Mizuno, Y. Miyamoto, L. Ottaviano, E. Semenova, P. Guan, D. Zibar, M. Galili, K. Yvind, T. Morioka, L. K. Oxenløwe, Single-source chip-based frequency comb enabling extreme parallel data transmission. *Nat. Photonics* **12**, 469–473 (2018).
 32. S. Jia, M.-C. Lo, L. Zhang, O. Ozolins, A. Udalcovs, D. Kong, X. Pang, R. Guzman, X. Yu, S. Xiao, S. Popov, J. Chen, G. Carpintero, T. Morioka, H. Hu, L. K. Oxenløwe, Integrated dual-laser photonic chip for high-purity carrier generation enabling ultrafast terahertz wireless communications. *Nat. Commun.* **13**, 1388 (2022).
 33. M. Troncoso-Costas, G. Jain, Y. Li, M. Patel, L. N. Venkatasubramani, S. O’Duill, F. Smyth, A. Ellis, F. Diaz-Otero, C. Browning, L. Barry, Experimental demonstration of 480 Gbit/s coherent transmission using a nanosecond switching tuneable laser. *Opt. Commun.* **554**, 130164 (2024).

Acknowledgments: The authors gratefully acknowledge the financial support from the Office of Naval Research (grant # N000142212531) and IET Harvey Engineering Research Prize. Yifan Zhao was supported by the Department of Energy (grant # DE-SC0016925).

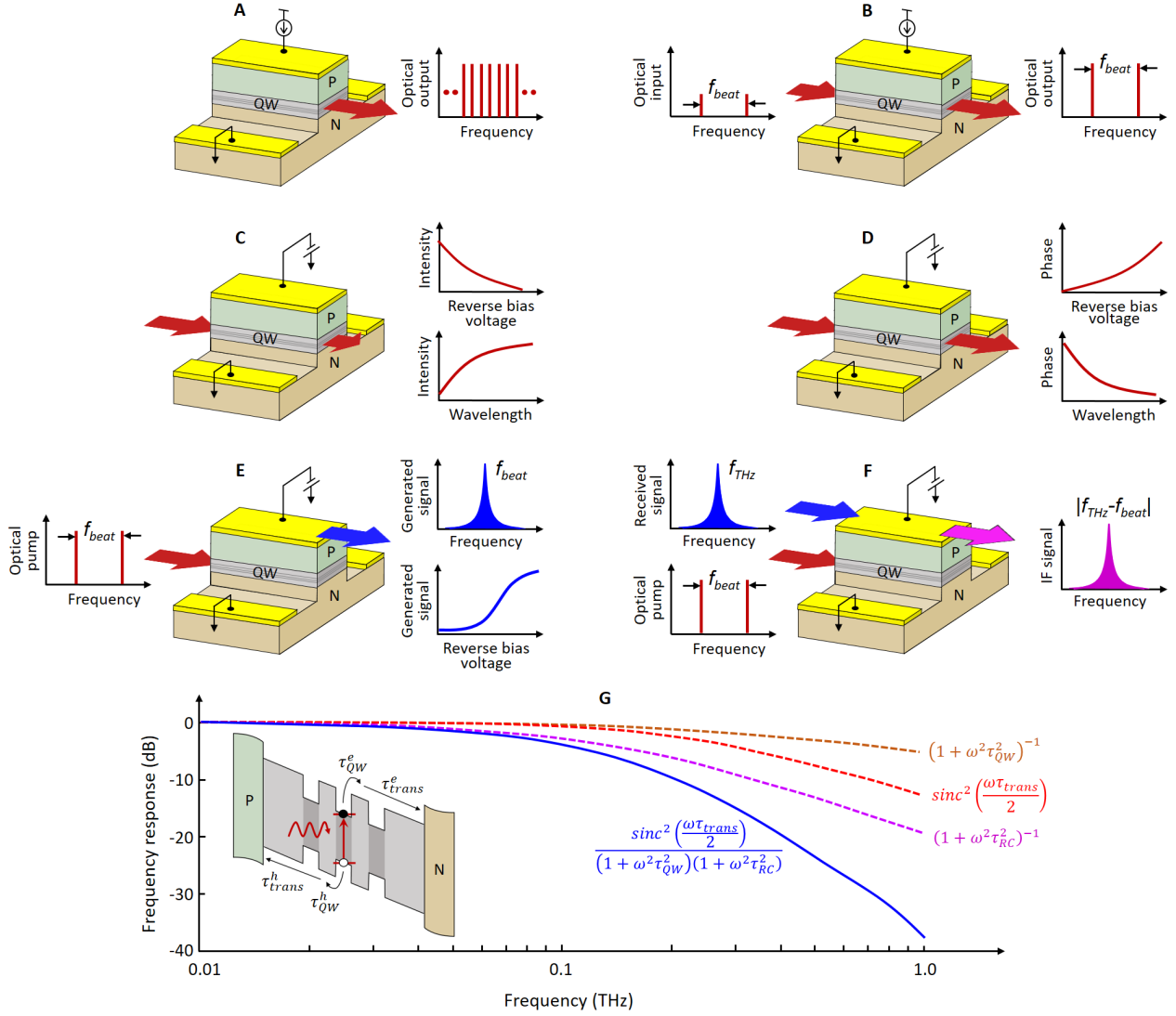


Fig. 1. The monolithically integrated terahertz optoelectronics (MITO) platform. The key building blocks of the MITO platform include: (A) optical pump source, (B) semiconductor optical amplifier, (C) intensity modulator, (D) phase modulator, (E) terahertz source, (F) and terahertz detector. (G) The theoretically predicted frequency response of the photomixing process that generates and detects terahertz signals for the photomixer structure shown in Fig. 2 is shown in blue. Here τ_{RC} represents the RC time-constant, τ_{trans} is the carrier transit time from the QWs to the P/N layers; and τ_{QW} is the carrier escape time from the QWs. These predictions assume that photo-generated electrons and holes transit through the depletion region at the saturation velocities $v_e=0.72 \times 10^7$ cm/s and $v_h=0.8 \times 10^7$ cm/s, respectively, for the QW heterostructures described in Supplementary Fig. S1. The estimated QW electron/hole escape times are 0.09 and 0.13 ps, respectively (29), with an RC time constant of 1.55 ps. The contributions of τ_{RC} , τ_{trans} , and τ_{QW} to the frequency response are shown in purple, red, and brown, respectively.

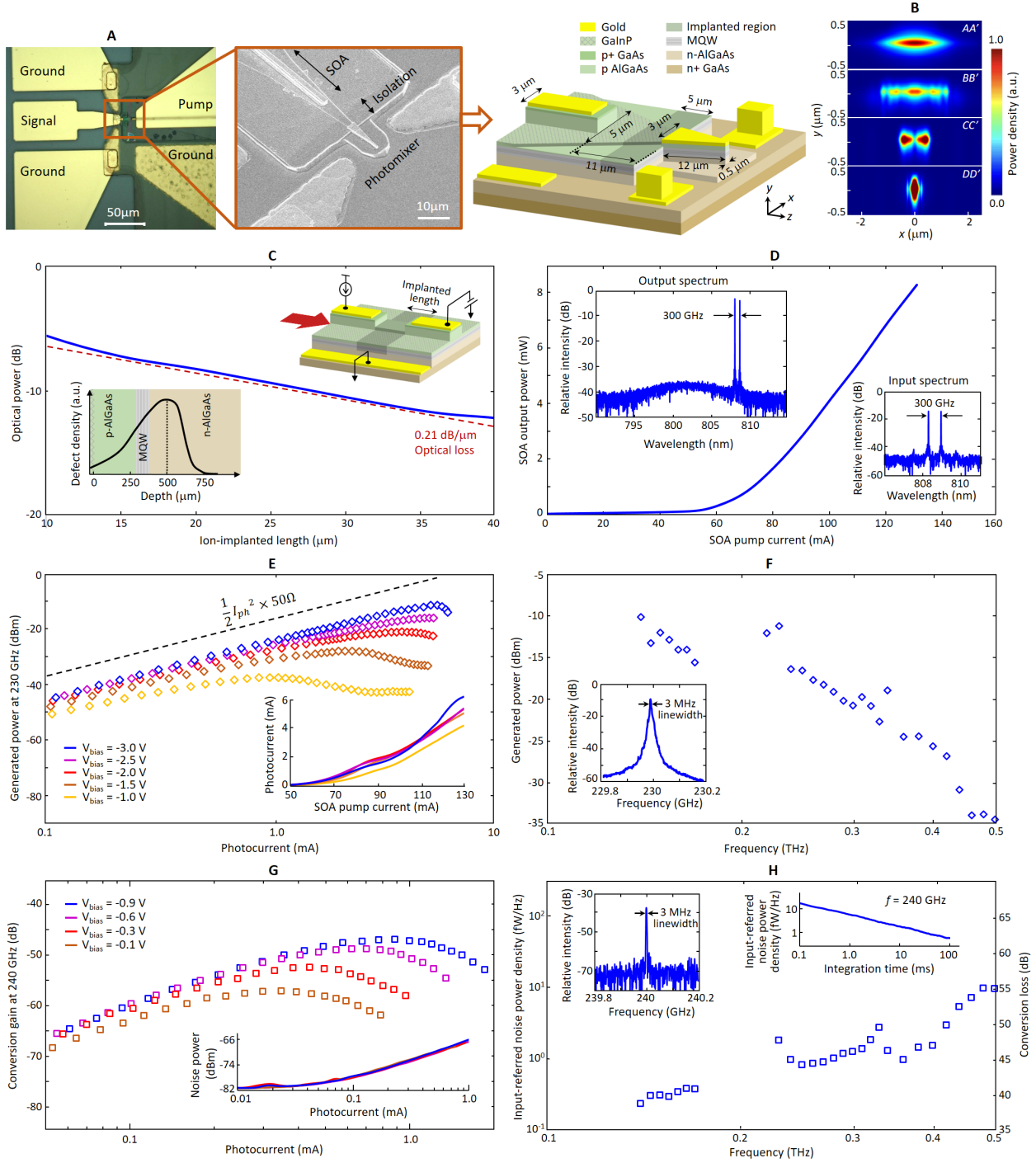


Fig. 2. Demonstration of integrated terahertz sources and detectors based on QW photomixers. (A) A fabricated terahertz source/detector prototype that generates/detects terahertz signals through photomixing in a GaAs/AlGaAs QW PIN photodiode. The photomixer waveguide has a tapered width ranging from 3 μm to 0.5 μm over a 12 μm length and is pumped by a monolithically integrated SOA ridge waveguide with a 3 μm ridge width. (B) The optical mode inside the SOA ridge waveguide (cross section AA') and at distances of 12/17/20 μm from the SOA output facet (cross sections BB'/CC'/DD'). Using electromagnetic simulations in Lumerical, we estimate an optical transmission of 97% through the tapered transition region and an optical absorption of 56.5% within the photomixer's active region. (C) To characterize the optical loss of the implanted electrical isolation region, we fabricated implanted test structures (top inset) with varying lengths and measured the transmitted optical power through them. The optical beam coupled to each implanted test structure is first amplified via propagation through a forward-biased PIN waveguide. The same waveguide is reverse biased during optical alignment to verify uniform coupling across all test structures using the measured photocurrent. The transmitted optical power through each implanted test structure is detected using a reverse-biased PIN waveguide. The bottom inset shows the simulated lattice defect density using SRIM software to ensure the implantation covers the

entire P-region. **(D)** SOA output power as a function of pump current for an input optical power of 0.15 mW at an 809 nm wavelength. Insets show the relative intensity of the SOA input and output spectra for an optical beat frequency of 300 GHz. **(E)** Generated power from the monolithically integrated terahertz source/detector with the SOA as a function of the photomixer photocurrent at 230 GHz. The inset shows the dependence of the photomixer photocurrent on the SOA pump current and the photomixer bias voltage. **(F)** Maximum generated power as a function of frequency at a bias voltage of -3 V. Power levels are measured using three different harmonic mixers and probes covering the frequency ranges 140-170 GHz, 230-330 GHz, and 340-500 GHz (see Methods). The abrupt power changes at the boundaries of these frequency ranges are due to deviations in the scattering parameters of the GSG probes, waveguide connections, and harmonic mixers used in the measurements. The inset shows the spectrum of the generated signal at 230 GHz. **(G)** Conversion gain of the monolithically integrated terahertz source/detector with the SOA as a function of the photomixer photocurrent at 240 GHz. The inset shows the dependence of the photomixer noise power on the photocurrent. **(H)** Conversion gain and input-referred noise power density at a bias voltage of -0.7 V, photocurrent of 0.38 mA, and an integration time of 25 ms. Inset shows the spectrum of the down-converted signal at 240 GHz and the dependence of the input-referred noise power density on the integration time at 240 GHz for a 10 kHz modulation frequency.

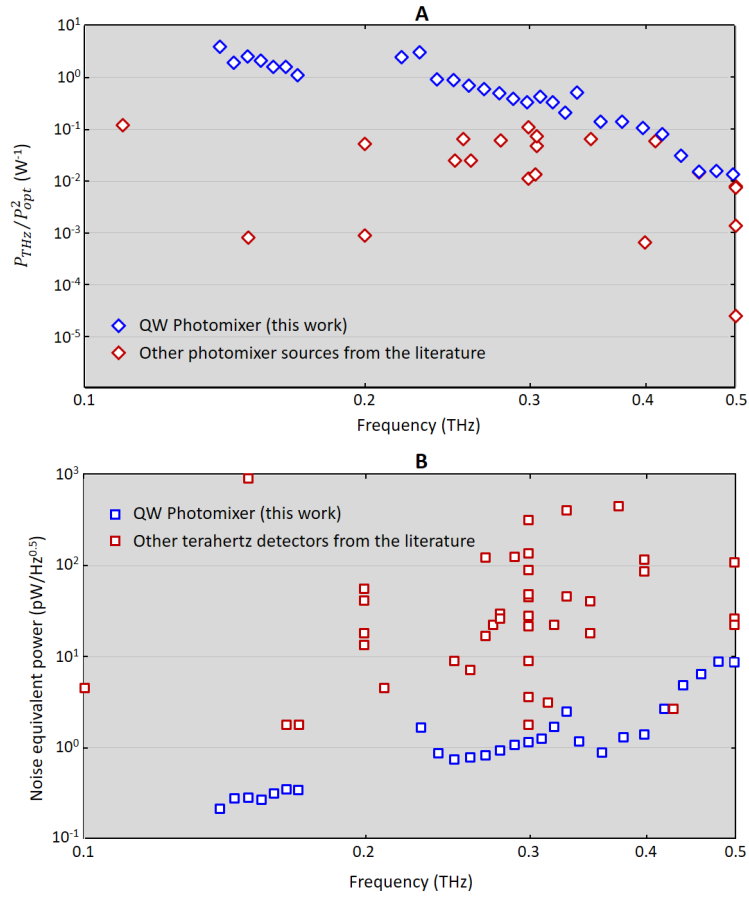


Fig. 3. Performance comparison with the state-of-the-art. (A) Comparison of the efficiency figure of merit P_{THz}/P_{opt}^2 for the demonstrated QW photomixer in terahertz generation mode with other photomixers from the literature, including those using free-space optical coupling from an external laser (see Supplementary Table S1). (B) Comparison of the noise-equivalent power of the demonstrated QW photomixer in terahertz detection mode with other room-temperature detectors from the literature, including those based on field-effect transistors, heterojunction bipolar transistors, high-electron-mobility transistors, Schottky diodes, and bolometers (see Supplementary Table S2).

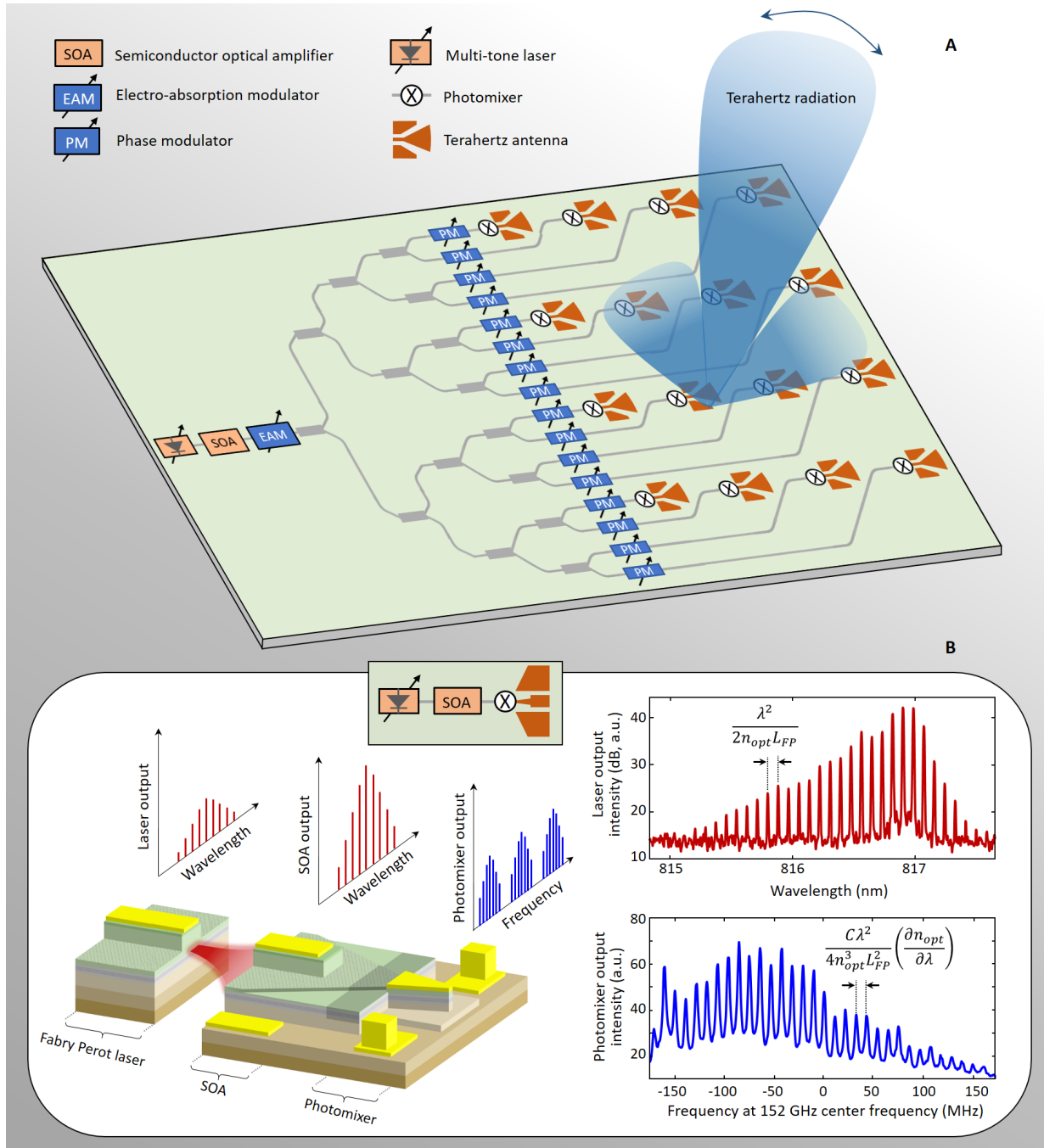


Fig. 4. Monolithically integrated terahertz optoelectronics platform based on QW structures. (A) Concept of a single-chip terahertz phased array transceiver for adaptive hyperspectral remote sensing and communication. One (or multiple) pairs of tunable lasers, with an adjustable terahertz frequency difference, are used to generate optical pump beams with one (or multiple) terahertz beat frequencies. These optical beams are amplified by one (or multiple) SOAs and distributed across an array of photomixers, which function as both terahertz transmitters and receivers. Depending on the system requirements, phase and intensity modulators are used to control the intensity and phase of the optical beams pumping each photomixer. For example, to implement communication systems, intensity modulators encode the terahertz carrier signal with data to be transmitted. Furthermore, to implement radar, remote sensing, and smart communication systems, which require spatial scanning of the transmitted terahertz radiation, an array of phase modulators dynamically controls the terahertz phase at each photomixer, enabling tilt in the phase front of the transmitted terahertz radiation. The platform also enables implementing spectrometry, spectroscopy, and hyperspectral imaging systems, as the radiated terahertz frequency can be easily tuned by adjusting the laser wavelengths. Furthermore, multi-channel terahertz communication systems can be implemented using orthogonal frequency division multiplexing by employing multiple optical pump beams with different terahertz beat frequencies. (B) A multi-mode terahertz transmitter realized using a Fabry-Perot laser, SOA, and photomixer on the same QW substrate. The measured multi-mode laser output for a Fabry-Perot cavity length of $L_{FP} = 1$ mm and the generated multi-mode signal around 152 GHz are shown by the red and blue curves, respectively.

Supplementary Materials

Material	Mole Fraction (x)	Thickness (nm)	Type	Doping level (cm ⁻³)	Description
GaAs		200	p-doped(C)	$>2 \times 10^{19}$	P-contact
Al(x)GaAs	0.55 to 0.05	50	p-doped(C)	$>3 \times 10^{18}$	
Al(x)GaAs	0.55	1250	p-doped(C)	1×10^{18}	P-cladding
GaIn(x)P	0.49	10	p-doped(Zn)	7×10^{17}	Etch stop
Al(x)GaAs	0.55	300	p-doped(C)	6×10^{17}	P-cladding
Al(x)GaAs	0.3	40	Undoped		Barrier
Al(x)GaAs	0.08	5.5	Undoped		QW
Al(x)GaAs	0.3	6	Undoped		Barrier
Al(x)GaAs	0.08	5.5	Undoped		QW
Al(x)GaAs	0.3	6	Undoped		Barrier
Al(x)GaAs	0.08	5.5	Undoped		QW
Al(x)GaAs	0.3	40	Undoped		Barrier
Al(x)GaAs	0.55	1500	n-doped(Si)	1×10^{18}	N-cladding
Al(x)GaAs	0.05 to 0.55	50	n-doped(Si)	2×10^{18}	N-cladding
GaAs		1000	n-doped(Si)	2×10^{18}	N-contact
SI-GaAs			Undoped		Substrate

Fig. S1. The GaAs/AlGaAs QW PIN photodiode heterostructure used for fabricating the terahertz source/detector prototypes is a commercially available design typically utilized in semiconductor lasers operating at an approximate wavelength of 800 nm. This structure was grown by Xiamen Powerway Advanced Material Co., Ltd (PAM-XIAMEN). From bottom to top, the structure comprises: a 1- μm -thick, highly doped n+ GaAs contact layer grown on a semi-insulating (SI) GaAs substrate; a 50-nm-thick graded AlGaAs layer, followed by a 1.5- μm -thick AlGaAs n-cladding layer; a 108.5-nm-thick intrinsic region; a 1.5- μm -thick AlGaAs p-cladding layer, which includes a 10-nm-thick lattice-matched GaInP etch stop layer positioned 300 nm above the intrinsic region; and another 50-nm-thick graded AlGaAs layer and a 200-nm-thick, highly doped p+ GaAs contact layer. Within the intrinsic region, there are three pairs of quantum wells, each consisting of a 5.5-nm-thick Al_{0.08}Ga_{0.92}As well layer and a 6-nm-thick Al_{0.3}Ga_{0.7}As barrier layer, flanked by a 40-nm-thick Al_{0.3}Ga_{0.7}As layer on each side. Although this wafer structure enables high-performance terahertz transmitter and receiver functionality, there remains potential for optimization to enhance its suitability for integrated terahertz optoelectronic applications.

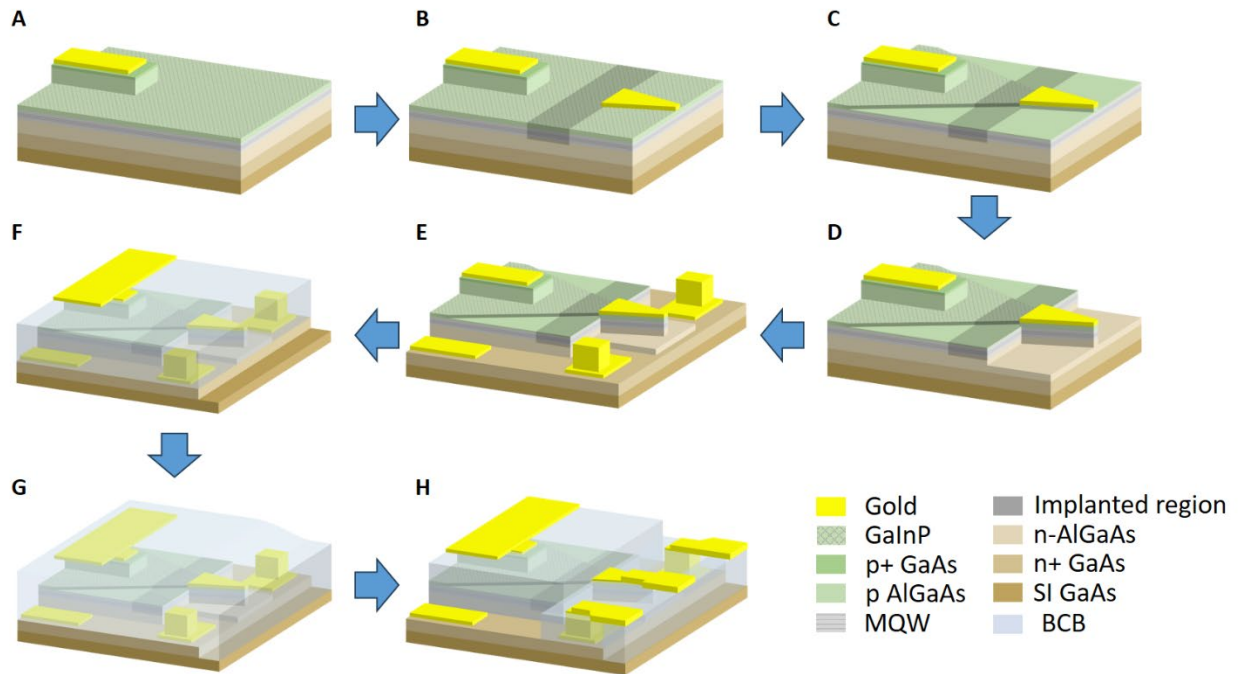


Fig. S2. The fabrication process for the terahertz source/detector prototype, which generates and detects terahertz signals via photomixing in a GaAs/AlGaAs QW PIN photodiode, involves the following steps: **(A)** Deposition of the SOA top contact and etching of the SOA waveguide. **(B)** Deposition of the photomixer top contact followed by ion implantation. **(C)** Etching of the shallow taper. **(D)** Etching of the photomixer waveguide. **(E)** Exposure of the n+ GaAs layer and deposition of the bottom contacts. **(F)** Spin coating with BCB (benzocyclobutene), followed by etch-back of BCB to allow deposition of the connection pad for the SOA top contact, and etching of the n+ GaAs in the GSG (ground-signal-ground) pad area. **(G)** Spin coating with BCB again. **(H)** Etch-back of BCB, deposition of GSG probing pads, and exposure of the SOA contact.

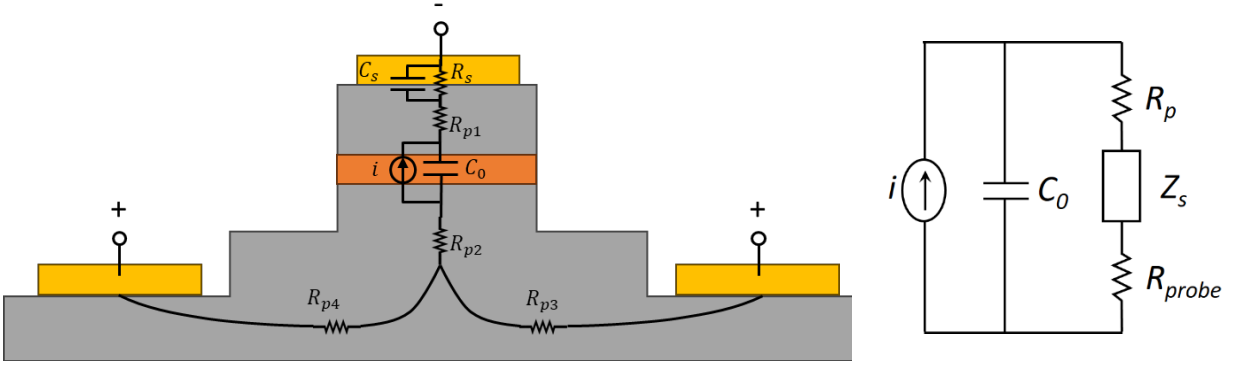


Fig. S3. The equivalent circuit model for the photomixer in terahertz generation mode is represented with the generated photocurrent modeled as a current source $i = I_{DC} + i_{THz} \cos(2\pi f_{beat}t)$, where I_{DC} and i_{THz} are the amplitudes of the DC and terahertz components of the photocurrent. Here, f_{beat} represents the terahertz beat frequency of the two optical tones pumping the photomixer. The terahertz photocurrent component is given by $i_{THz} \cong i_{DC} \cdot \text{sinc}(\pi f_{beat} \tau_{trans}) (1 + j2\pi f_{beat} \tau_{QW})^{-1}$, where τ_{trans} is the effective carrier transit time from the QWs to the P/N layers, and τ_{QW} is the effective carrier escape time from the QWs. The current source is in parallel with the PIN diode depletion region capacitance C_0 and this combination is in series with the 50Ω resistance of the GSG probe, R_{probe} , the parasitic resistance R_p from the n and p regions, and the Schottky contact impedance Z_s . The terahertz current passing through the load resistance is thus: $i_L = i_{THz} [1 + j2\pi f_{beat} C_0 (R_{probe} + R_p + Z_s)]^{-1} = i_{THz} [1 + j2\pi f_{beat} \tau_{RC}]^{-1}$ and the generated terahertz power is $\frac{1}{2} |i_L|^2 R_{probe}$, where τ_{RC} represents the photomixer RC time constant, estimated to be 1.55 ps for the designed photomixer shown in Fig. 2.

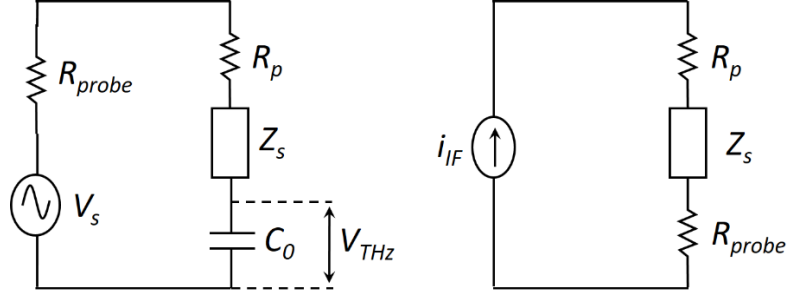


Fig. S4. The equivalent circuit model for the photomixer in terahertz detection mode includes a voltage source V_s and the $50\ \Omega$ resistance of the GSG probe, R_{probe} , to represent the terahertz signal input. These components are in series with the parasitic resistance R_p from the n and p regions, the Schottky contact impedance Z_s , and the capacitance C_0 of the PIN diode depletion region. For a received terahertz power $P_{THz} = \frac{V_s^2}{8R_{probe}}$, the induced voltage across the intrinsic region is calculated as $V_{THz} = V_s [1 + j2\pi f_{beat} C_0 (R_{probe} + R_p + Z_s)]^{-1}$. As described previously, the photocurrent of the photomixer has both DC and terahertz components, represented by $i = I_{DC} + i_{THz} \cos(2\pi f_{beat} t)$, where $i_{THz} \cong i_{DC} \cdot \text{sinc}(\pi f_{beat} \tau_{trans}) (1 + j2\pi f_{beat} \tau_{QW})^{-1} = i_{DC} \cdot H_{carrier}(2\pi f_{beat})$. In terahertz detection mode, the voltage applied to the intrinsic region, $V_{DC} + V_{THz} \cos(2\pi f_{THz} t)$, consists of a DC component from the device's DC bias and a terahertz component, V_{THz} , induced across the intrinsic region of the photomixer at frequency f_{THz} . Assuming $V_{THz} \ll V_{DC}$, the induced photocurrent is given by $i = I_{DC} + I_{DC} * H_{carrier}(V_{DC} + V_{THz} \cos(2\pi f_{beat} t)) * \cos(2\pi f_{THz} t)$, approximated as $I_{DC} + I_{DC} * [H_{carrier}(V_{DC}) + H'_{carrier}(V_{DC}) * V_{THz} \cos(2\pi f_{THz} t)] * \cos(2\pi f_{beat} t)$, yielding an intermediate frequency (IF) component of $\frac{1}{2} I_{DC} * H'_{carrier}(V_{DC}) * V_{THz} \cos|2\pi f_{beat} t - 2\pi f_{THz} t|$. Thus, the magnitude of the IF current is $i_{IF} = \frac{1}{2} I_{DC} V_s * H'_{carrier}(V_{DC}) [1 + j2\pi f_{beat} C_0 (R_{probe} + R_p + Z_s)]^{-1}$. The conversion gain of the terahertz detector, defined as the down-converted IF power, $\frac{1}{2} i_{IF}^2 R_{probe}$, divided by the received terahertz power, P_{THz} , is given by $[I_{DC} R_{probe} * H'_{carrier}(V_{DC})]^2 [1 + j2\pi f_{beat} C_0 (R_{probe} + R_p + Z_s)]^{-2}$, where $H'_{carrier}(V_{DC})$ is proportional to $\text{sinc}(\pi f_{beat} \tau_{trans}) (1 + j2\pi f_{beat} \tau_{QW})^{-1}$.

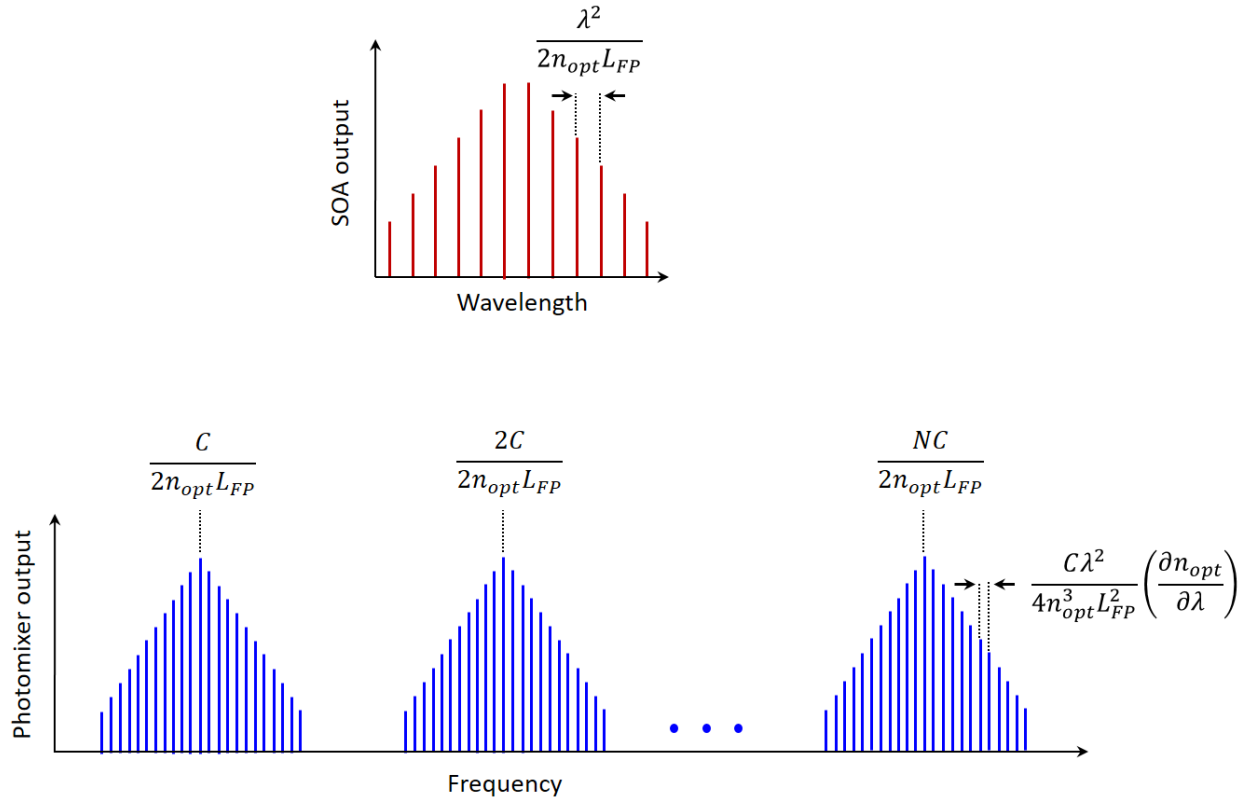


Fig. S5. The multi-mode signal generated by the photomixer (blue graph) in response to the multi-mode optical emission (red graph) from the Fabry-Perot laser. The optical tones have a wavelength spacing of $\frac{\lambda^2}{2n_{opt}L_{FP}}$, where λ is the optical wavelength, n_{opt} is the effective optical index in the laser cavity, and L_{FP} is the length of the Fabry-Perot cavity. The signal generated by the photomixing process consists of multi-mode tones centered at frequencies of $i \frac{C}{2n_{opt}L_{FP}}$, with a frequency spacing of $\frac{C\lambda^2}{4n_{opt}^3L_{FP}^2} \left(\frac{\partial n_{opt}}{\partial \lambda} \right)$, where C is the speed of light, $i = 1, 2, 3, \dots$, and $\frac{\partial n_{opt}}{\partial \lambda}$ represents the dispersion of the optical index inside the laser cavity.

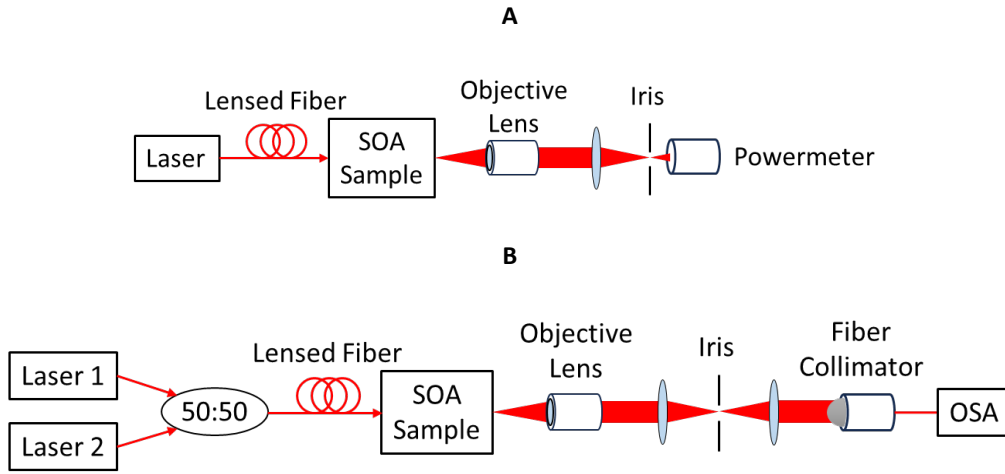


Fig. S6. The experimental setups used to characterize the output power and spectral properties of the SOA are shown in (A) and (B), respectively.

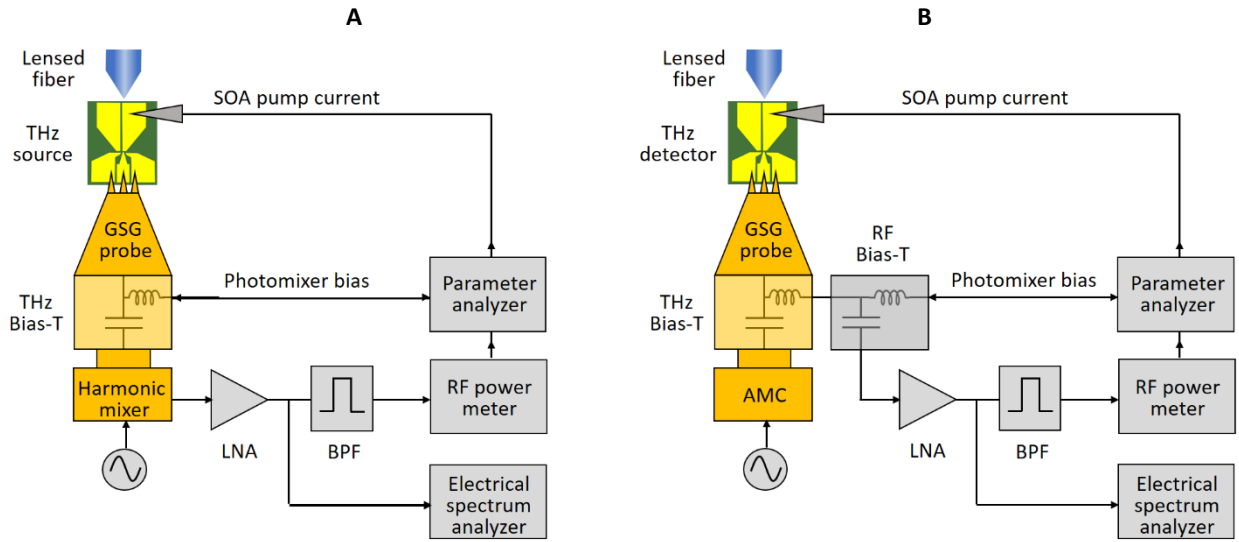


Fig. S7. The experimental setups used to characterize the terahertz sources and detectors are shown in (A) and (B), respectively.

Reference	Frequency (GHz)	P_{opt} (mW)	P_{THz} (mW)
D. Stanze, A. Deninger, A. Roggenbuck, S. Schindler, M. Schlak, B. Sartorius, Compact cw terahertz spectrometer pumped at 1.5 μm wavelength. J Infrared Milli Terahz Waves 32, 225–232 (2011).	500	25	0.005
E. Rouvalis, C. C. Renaud, D. G. Moodie, M. J. Robertson, A. J. Seeds, Continuous wave terahertz generation from ultra-fast InP-based photodiodes. IEEE Transactions on Microwave Theory and Techniques 60, 509–517 (2012).	306	48.1 / 38.7	0.11
E. Rouvalis, C. C. Renaud, D. G. Moodie, M. J. Robertson, A. J. Seeds, Traveling-wave Uni-Traveling Carrier Photodiodes for continuous wave THz generation. Opt. Express 18, 11105–11110 (2010).	457 / 255	100 / 40	0.148 / 0.105
J.-M. Wun, H.-Y. Liu, Y.-L. Zeng, S.-D. Yang, C.-L. Pan, C.-B. Huang, J.-W. Shi, Photonic high-power continuous wave THz-wave generation by Using Flip-Chip Packaged Uni-Traveling Carrier Photodiodes and a Femtosecond Optical Pulse Generator. J. Lightwave Technol. 34, 1387–1397 (2016).	280	130	1.04
V. Rymanov, A. Stöhr, S. Dülme, T. Tekin, Triple transit region photodiodes (TTR-PDs) providing high millimeter wave output power. Opt. Express 22, 7550–7558 (2014).	110	94	1.05
I. D. Henning, M. J. Adams, Y. Sun, D. G. Moodie, D. C. Rogers, P. J. Cannard, S. “Jeevan” Dosanjh, M. Skuse, R. J. Firth, Broadband Antenna-Integrated, Edge-Coupled Photomixers for Tuneable Terahertz Sources. IEEE J. Quantum Electron. 46, 1498–1505 (2010).	410	50	0.15
A. Wakatsuki, T. Furuta, Y. Muramoto, T. Yoshimatsu, H. Ito, “High-power and broadband sub-terahertz wave generation using a J-band photomixer module with rectangular-waveguide output port” in 2008 33rd International Conference on Infrared, Millimeter and Terahertz Waves (IEEE, 2008), pp. 1–2.	350	91	0.54
H. Ito, T. Yoshimatsu, H. Yamamoto, T. Ishibashi, Widely Frequency Tunable Terahertz-Wave Emitter Integrating Uni-Traveling-Carrier Photodiode and Extended Bowtie Antenna. Appl. Phys. Express 6, 064101 (2013).	200 / 500	47.6 / 47.6	0.12 / 0.017
P. Latzel, F. Pavanello, M. Billet, S. Bretin, A. Beck, M. Vanwollegem, C. Coinon, X. Wallart, E. Peytavit, G. Ducournau, M. Zaknour, J.-F. Lampin, Generation of mW Level in the 300-GHz Band Using Resonant-Cavity-Enhanced Unitraveling Carrier Photodiodes. IEEE Trans. THz Sci. Technol. 7, 800–807 (2017).	300	83	0.75
J.-M. Wun, C.-H. Lai, N.-W. Chen, J. E. Bowers, J.-W. Shi, Flip-Chip Bonding Packaged THz Photodiode With Broadband High-Power Performance. IEEE Photon. Technol. Lett. 26, 2462–2464 (2014).	260	162.5	0.67
J. Mangeney, A. Merigault, N. Zerounian, P. Crozat, K. Blary, J. F. Lampin, Continuous wave terahertz generation up to 2THz by photomixing on ion-irradiated In _{0.53} Ga _{0.47} As at 1.55 μm wavelengths. Applied Physics Letters 91, 241102 (2007).	500	40	0.00004
S.-H. Yang, M. Jarrahi, “High-power continuous-wave terahertz generation through plasmonic photomixers” in 2016 IEEE MTT-S International Microwave Symposium (IMS) (IEEE, 2016), pp. 1–4.	150	350	0.1
H. Tanoto, J. H. Teng, Q. Y. Wu, M. Sun, Z. N. Chen, S. A. Maier, B. Wang, C. C. Chum, G. Y. Si, A. J. Danner, S. J. Chua, Greatly enhanced continuous-wave terahertz	300 / 500	90 / 90	0.09 / 0.011

emission by nano-electrodes in a photoconductive photomixer. <i>Nature Photon</i> 6, 121–126 (2012).			
N. Khiabani, Y. Huang, L. E. Garcia-Munoz, Y.-C. Shen, A. Rivera-Lavado, A Novel Sub-THz Photomixer With Nano-Trapezoidal Electrodes. <i>IEEE Trans. THz Sci. Technol.</i> 4, 501–508 (2014).	200 / 400	30 /30	0.0008 / 0.0006
E. Peytavit, S. Lepilliet, F. Hindle, C. Coinon, T. Akalin, G. Ducournau, G. Mouret, J.-F. Lampin, Milliwatt-level output power in the sub-terahertz range generated by photomixing in a GaAs photoconductor. <i>Applied Physics Letters</i> 99, 223508 (2011).	305	162	0.35
E. Peytavit, P. Latzel, F. Pavanello, G. Ducournau, J.-F. Lampin, CW Source Based on Photomixing With Output Power Reaching 1.8 mW at 250 GHz. <i>IEEE Electron Device Lett.</i> 34, 1277–1279 (2013).	250	270	1.8

Table S1. The generated power as a function of the optical pump power for photomixer sources demonstrated in the literature over the 100-500 GHz frequency range, including those with free-space optical coupling from an external laser.

Reference	Type	NEP (pW/Hz ^{0.5})	Frequency (GHz)
M. W. Ryu, J. S. Lee, K. S. Kim, K. Park, J.-R. Yang, S.-T. Han, K. R. Kim, High-Performance Plasmonic THz Detector Based on Asymmetric FET With Vertically Integrated Antenna in CMOS Technology. <i>IEEE Trans. Electron Devices</i> 63, 1742–1748 (2016).	FET	15	200
E. Shaulov, S. Jameson, E. Socher, A Zero Bias J-Band Antenna-Coupled Detector in 65-nm CMOS. <i>IEEE Trans. THz Sci. Technol.</i> 11, 62–69 (2021).	FET	3.5	315
L. Liu, J. L. Hesler, H. Xu, A. W. Lichtenberger, R. M. Weikle, A Broadband Quasi-Optical Terahertz Detector Utilizing a Zero Bias Schottky Diode. <i>IEEE Microw. Wireless Compon. Lett.</i> 20, 504–506 (2010).	SBD	5/20	210/350
N. Daghestani, K. Parow-Souchon, D. Pardo, H. Liu, N. Brewster, M. Frogley, G. Cinque, B. Alderman, P. G. Huggard, Room temperature ultrafast InGaAs Schottky diode based detectors for terahertz spectroscopy. <i>Infrared Physics & Technology</i> 99, 240–247 (2019).	SBD	5/50	100/300
S. V. Berkel, E. S. Malotau, C. D. Martino, M. Spirito, D. Cavallo, A. Neto, N. Lombart, Wideband Modeling of CMOS Schottky Barrier Diode Detectors for THz Radiometry. <i>IEEE Trans. THz Sci. Technol.</i> 11, 495–507 (2021).	SBD	20/50/95/120	200/300/400/500
J. Yun, S. J. Oh, K. Song, D. Yoon, H. Y. Son, Y. Choi, Y.-M. Huh, J.-S. Rieh, Terahertz Reflection-Mode Biological Imaging Based on InP HBT Source and Detector. <i>IEEE Trans. THz Sci. Technol.</i> 7, 274–283 (2017).	InP HBT	25/45	275/350
H. Qin, J. Sun, S. Liang, X. Li, X. Yang, Z. He, C. Yu, Z. Feng, Room-temperature, low-impedance and high-sensitivity terahertz direct detector based on bilayer graphene field-effect transistor. <i>Carbon</i> 116, 760–765 (2017).	Graphene FET	51	330
S. Kim, M. I. W. Khan, D.-W. Park, S.-G. Lee, K. R. Kim, Effects of Parasitic Source/Drain Junction Area on Terahertz Responsivity of MOSFET Detector. <i>IEEE Trans. THz Sci. Technol.</i> 8, 681–687 (2018).	FET	54	300
M. I. W. Khan, S. Kim, D.-W. Park, H.-J. Kim, S.-K. Han, S.-G. Lee, Nonlinear Analysis of Nonresonant THz Response of MOSFET and Implementation of a High-Responsivity Cross-Coupled THz Detector. <i>IEEE Trans. THz Sci. Technol.</i> 8, 108–120 (2018).	FET	29	500
H.-J. Lee, S.-T. Han, J.-R. Yang, CMOS Plasmon Detector with Three Different Body-Biasing MOSFETs. <i>IEEE Access</i> 8, 215840–215850 (2020).	FET	62	200
X. Yang, A. Vorobiev, K. Jeppson, J. Stake, Describing Broadband Terahertz Response of Graphene FET Detectors by a Classical Model. <i>IEEE Trans. THz Sci. Technol.</i> 10, 158–166 (2020).	FET	24	300
G.-E. Lee, H.-J. Lee, S.-T. Han, J.-R. Yang, CMOS Detector Using Customized Bolt-Wrench Capacitor on Backend Oxide Layer. <i>IEEE Microw. Wireless Compon. Lett.</i> 31, 1012–1015 (2021).	FET	46	200
M. W. Mansha, T. E. Rice, M. A. Oehlschlaeger, I. Wilke, M. M. Hella, A 220–300 GHz Twin-FET Detector for Rotational Spectroscopy of Gas Mixtures. <i>IEEE Sensors J.</i> 21, 4553–4562 (2021).	FET	10	250

E. Javadi, A. Lisauskas, M. Shahabadi, N. Masoumi, J. Zhang, J. Matukas, H. G. Roskos, Terahertz Detection With a Low-Cost Packaged GaAs High-Electron-Mobility Transistor. <i>IEEE Trans. THz Sci. Technol.</i> 9, 27–37 (2019).	HEMT	135	270
M. Andree, J. Grzyb, R. Jain, B. Heinemann, U. R. Pfeiffer, Broadband Modeling, Analysis, and Characterization of SiGe HBT Terahertz Direct Detectors. <i>IEEE Trans. Microwave Theory Techn.</i> 70, 1314–1333 (2022).	HBT	2	300
K. Sengupta, D. Seo, L. Yang, A. Hajimiri, Silicon Integrated 280 GHz Imaging Chipset With 4×4 SiGe Receiver Array and CMOS Source. <i>IEEE Trans. THz Sci. Technol.</i> 5, 427–437 (2015).	SiGe transistor	8	260
Z. Li, B. Qi, X. Zhang, S. Zeinolabedinzadeh, L. Sang, J. D. Cressler, A 0.32-THz SiGe Imaging Array With Polarization Diversity. <i>IEEE Trans. THz Sci. Technol.</i> 8, 215–223 (2018).	SiGe HBT	25	320
M. Andree, J. Grzyb, R. Jain, B. Heinemann, U. R. Pfeiffer, “A Broadband Dual-Polarized Terahertz Direct Detector in a 0.13- μm SiGe HBT Technology” in 2019 IEEE MTT-S International Microwave Symposium (IMS) (IEEE, 2019), pp. 500–503.	SiGe HBT	3	430
A. A. Generalov, M. A. Andersson, X. Yang, A. Vorobiev, J. Stake, A 400-GHz Graphene FET Detector. <i>IEEE Trans. THz Sci. Technol.</i> 7, 614–616 (2017).	Graphene FET	130	400
A. Boukhayma, A. Dupret, J.-P. Rostaing, C. Enz, A Low-Noise CMOS THz Imager Based on Source Modulation and an In-Pixel High-Q Passive Switched-Capacitor N-Path Filter. <i>Sensors</i> 16, 325 (2016).	FET	18.7	270
K. Ikamas, J. Zdanevicius, L. Dundulis, S. Pralgauskaite, A. Lisauskas, D. Cibiraite, D. Voss, V. Krozer, H. G. Roskos, “Quasi optical THz detectors in Si CMOS” in 2018 22nd International Microwave and Radar Conference (MIKON) (IEEE, 2018), pp. 719–721.	FET	31	300
M. Uzunkol, J. M. Edwards, G. M. Rebeiz, “A 0.3 THz 4 × 4 cold-FET imaging array in 45 nm CMOS SOI” in 2014 IEEE MTT-S International Microwave Symposium (IMS2014) (IEEE, 2014), pp. 1–4.	FET	100	300
S. Cherednichenko, A. Hammar, S. Bevilacqua, V. Drakinskiy, J. Stake, A. Kalabukhov, A Room Temperature Bolometer for Terahertz Coherent and Incoherent Detection. <i>IEEE Trans. Terahertz Sci. Technol.</i> 1, 395–402 (2011).	Bolometer	450	330
D. P. Neikirk, W. W. Lam, D. B. Rutledge, Far-infrared microbolometer detectors. <i>Int J Infrared Milli Waves</i> 5, 245–278 (1984).	Bolometer	150	300
P. P. Tong, D. P. Neikirk, P. E. Young, W. A. Peebles, N. C. Luhmann, D. B. Rutledge, Imaging Polarimeter Arrays for Near-Millimeter Waves. <i>IEEE Transactions on Microwave Theory and Techniques</i> 32, 507–512 (1984).	Bolometer	500	375
S. M. Rahman, Z. Jiang, Md. I. B. Shams, P. Fay, L. Liu, A G-Band Monolithically Integrated Quasi-Optical Zero-Bias Detector Based on Heterostructure Backward Diodes Using Submicrometer Airbridges.	HBD	2	170

IEEE Trans. Microwave Theory Techn. 66, 2010–2017 (2018).			
D. Yoon, J. Kim, J. Yun, M. Kaynak, B. Tillack, J.-S. Rieh, 300-GHz Direct and Heterodyne Active Imagers Based on 0.13- μm SiGe HBT Technology. IEEE Trans. THz Sci. Technol. 7, 536–545 (2017).	SiGe HBT	4	300
R. Han, Y. Zhang, D. Coquillat, H. Videlier, W. Knap, E. Brown, K. K. O, A 280-GHz Schottky Diode Detector in 130-nm Digital CMOS. IEEE J. Solid-State Circuits 46, 2602–2612 (2011).	SBD	33	280
J. L. Hesler, T. W. Crowe, “NEP and responsivity of THz zero-bias Schottky diode detectors” in 2007 Joint 32nd International Conference on Infrared and Millimeter Waves and the 15th International Conference on Terahertz Electronics (IEEE, 2007), pp. 844–845.	SBD	2	165
F. Schuster, D. Coquillat, H. Videlier, M. Sakowicz, F. Teppe, L. Dussopt, B. Giffard, T. Skotnicki, W. Knap, Broadband terahertz imaging with highly sensitive silicon CMOS detectors. Opt. Express 19, 7827–7832 (2011).	FET	10	300
M. Bauer, A. Ramer, S. A. Chevtchenko, K. Y. Osipov, D. Cibraite, S. Pralgauskaite, K. Ikamas, A. Lisauskas, W. Heinrich, V. Krozer, H. G. Roskos, A High-Sensitivity AlGaIn/GaN HEMT Terahertz Detector With Integrated Broadband Bow-Tie Antenna. IEEE Trans. THz Sci. Technol. 9, 430–444 (2019).	HEMT	25	500
O. Cojocari, N. Sobornytssky, C. Weickmann, R. Jakoby, A. Semenov, H. Hübers, R. Müller, A. Hoehl, “Quasi optical Schottky diode detectors for fast ultra-wideband detection” in 2016 IEEE International Conference on Microwave and Millimeter Wave Technology (ICMMT) (IEEE, 2016), pp. 52–53.	PTE	1000	150
W. Guo, L. Wang, X. Chen, C. Liu, W. Tang, C. Guo, J. Wang, W. Lu, Graphene-based broadband terahertz detector integrated with a square-spiral antenna. Opt. Lett. 43, 1647–1650 (2018).	PTE	350	300
W. Guo, Z. Dong, Y. Xu, C. Liu, D. Wei, L. Zhang, X. Shi, C. Guo, H. Xu, G. Chen, L. Wang, K. Zhang, X. Chen, W. Lu, Sensitive Terahertz Detection and Imaging Driven by the Photothermoelectric Effect in Ultrashort - Channel Black Phosphorus Devices. Advanced Science 7, 1902699 (2020).	PTE	138	290
R. Han, Y. Zhang, Y. Kim, D. Y. Kim, H. Shichijo, E. Afshari, K. K. O, Active Terahertz Imaging Using Schottky Diodes in CMOS: Array and 860-GHz Pixel. IEEE J. Solid-State Circuits 48, 2296–2308 (2013).	SBD	29	280

Table S2. The noise-equivalent power of room-temperature detectors demonstrated in the literature over the 100-500 GHz range, including those based on field-effect transistors (FETs), heterojunction bipolar transistors (HBTs), high-electron-mobility transistors (HEMTs), Schottky barrier diodes (SBDs), bolometers, heterostructure backward diodes (HBDs), and photo-thermoelectric (PTE) detectors.